

CrossMark
click for updatesCite this: *J. Mater. Chem. A*, 2015, 3,
4659

Ag-encapsulated Au plasmonic nanorods for enhanced dye-sensitized solar cell performance†

Hua Dong,^a Zhaoxin Wu,^{*a} Ahmed El-Shafei,^b Bin Xia,^a Jun Xi,^a Shuya Ning,^a Bo Jiao^a
and Xun Hou^a

In this article, Ag-encapsulated Au nanorods (Au@Ag NRs) are prepared and introduced into dye-sensitized solar cells (DSSCs). As a unique plasmonic nanostructure, this composite exhibits the superiorities of enhanced light-harvesting as well as restrained charge recombination of DSSCs. Remarkably, the enhanced light absorption of the photoanode can be obtained *via* the surface plasmon resonance (SPR) effect of the Au@Ag NRs, whereas a broadened absorption in the red and near-infrared (NIR) region ensures the full utilization of the solar energy. Beyond the dominated optical utility, the presence of the Au@Ag NRs promotes the suppression of the charge recombination, further enhancing the photochemical catalysis of DSSCs. An optimized Au@Ag NR modified DSSC is achieved with a power conversion efficiency of 8.43%, which is significantly superior to that of the pure TiO₂ DSSC with a PCE of 5.91%.

Received 28th September 2014
Accepted 7th January 2015

DOI: 10.1039/c4ta05154h

www.rsc.org/MaterialsA

1. Introduction

Recently, dye-sensitized solar cells (DSSCs) have attracted significant attention and reach up to 13% power conversion efficiency.^{1,2} Due to its easy fabrication, low cost and high photon-to-electric power conversion efficiency, this type of cell has been expected to be a potential alternative to conventional silicon-based solar cells.^{3,4} Extending the response of dye sensitizers to a broader range of the solar spectrum and improving the light-harvesting efficiency (LHE) of the photoanode are the critical factors to improve the performance of DSSCs.⁵ Therefore, to obtain a higher efficiency, considerable efforts on the dye-adsorbed photoanode have been explored, which mainly focused on the design of new dye molecules and the structure-modified technology of the photoanode films.

Over 90% energy of the sunlight is concentrated in visible and near-infrared (NIR) region;⁶ thus, a high-efficiency sensitizer applied in DSSCs is expected to exhibit a wide absorption spectrum. Presently, most of the universal sensitizers, such as N3, N719 and C106,⁷ could only make effective use of the sunlight in the region of 400–650 nm. The rather low utilization of red and NIR region limit the light harvesting efficiency at longer wavelengths, which appears to be a bottleneck of the

device efficiency. Recently, new sensitizers were designed to extend the absorption to the red or NIR region.^{8–10} However, the overall efficiency was not improved because of the decreased availability of the new dyes at the short wavelength. Co-sensitization was another approach to fully utilize the energy of the sunlight,^{11,12} whereas the complexity of the fabrication process and the match of the energy level at sensitizer/semiconductor interface remains unsolved perfectly. As a consequence, keeping the strong absorption at the visible region as well as increasing the harvesting at longer wavelength is the most suitable development tendency.

Based on the conventional sensitizers, the surface plasmon resonance (SPR) effect was recently employed as an attractive approach to increase light harvesting efficiency.^{13,14} Plasmonic metal-nanoparticles, such as Ag nanoparticles, Au nanoparticles, and core-shell nanostructures, could boost the performance of the DSSCs *via* the SPR effect.^{15–22} SPR is a collective oscillation of conduction band electrons in a metal nanoparticle driven by the electromagnetic field of incident light, which could significantly increase the light absorption of the dye and the generation of the photon-carriers. However, the absorption spectrum of the reported plasmonic particles is located in the short wavelength of the visible light. Actually, the reported plasmonic applications could only enhance the LHE to some extent, and the limitation is that the improvement of LHE was just presented at a relatively narrow range.^{23,24}

To achieve a win-win course of both enhancing the response of sensitizers and extending the light harvesting region of the photoanode, the preferable choice is the development of novel plasmonic nanocomposites with extensive absorption spectra. In this article, unique (Au core)–(Ag shell) nanorods (Au@Ag

^aKey Laboratory of Photonics Technology for Information, Key Laboratory for Physical Electronics and Devices of the Ministry of Education, School of Electronic and Information Engineering, Xi'an Jiaotong University, Xi'an 710049, P. R. China. E-mail: zhaoxinwu@mail.xjtu.edu.cn; Tel: +86-29-82664867

^bPolymer and Color Chemistry Program, North Carolina State University, Raleigh, NC 27695, USA. E-mail: ahmed_el-shafei@ncsu.edu

† Electronic supplementary information (ESI) available. See DOI: 10.1039/c4ta05154h

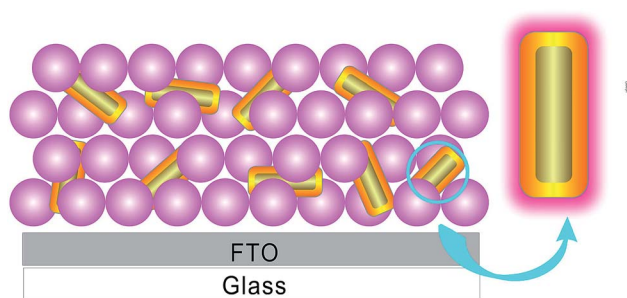


Fig. 1 Schematic structure of DSSCs with Au@Ag NRs incorporated in a TiO₂ film.

NRs) were explored and applied in the photoanode of DSSCs, as shown schematically in Fig. 1. “Rod-like” metal nanostructures have a tunable longitudinal and transverse plasmon absorption from visible to the NIR region, which could provide a unique opportunity for utilizing the low energy range of the solar energy.²⁵ The coupling effect between Ag and Au exhibit much stronger electric field enhancements than those of pure Au nanostructures, which achieved a rather wide plasmonic wavelength from 350 to 900 nm with four strong SPR peaks. With the introduction of the Au@Ag NRs, both the increased absorption of dye and broadened absorption region of the photoanode were achieved. In addition to the primary contributions on LHE, the Au@Ag NRs present the capability of suppressing the charge recombination, which could further improve the performance of the DSSCs. Considering the stability and easily-modified process, the prospect of this type of nanorods is brilliant for its future application.

2. Results and discussion

2.1. Properties of the bristled Au@Ag NRs

Fig. 2a and b show the TEM images of the Au@Ag NRs, and Fig. 2c shows the SEM image of the Au@Ag NRs. It can be seen that the Au@Ag NRs have narrow shape and size distributions. The average length and diameter of Au core are 65 ± 4 nm and 15 ± 2 nm, and the two parameters of Ag shell are 70 ± 5 nm and 28 ± 3 nm, respectively. EDX spectrum was used to analyze the content of the Au@Ag NRs, and the Ag and Au peaks were clearly observed (shown in Fig. S1†).

The preparation of elongated anisotropic Ag nanostructures with uniform shape and narrow size distributions has been proven to be challenging.²⁶ Au nanorods, due to the attractive advantages, such as facile growth process, tunable-longitudinal plasmon wavelengths, and chemical stability, could function as excellent supports for the formation of Ag shells.²⁷ The synthetic (Au core)–(Ag shell) nanorods were expected to exhibit specific plasmonic bands determined by the coupling effect between Ag and Au. Moreover, the plasmon wavelengths range can be tailored in the visible to near-infrared regions by varying the Au core size and the Ag shell thickness.^{28,29}

Obtaining an appropriate plasmonic wavelength of the metal nanorods is important to achieve highly efficient plasmonic DSSCs. The absorption peak of metal nanostructures, that is,

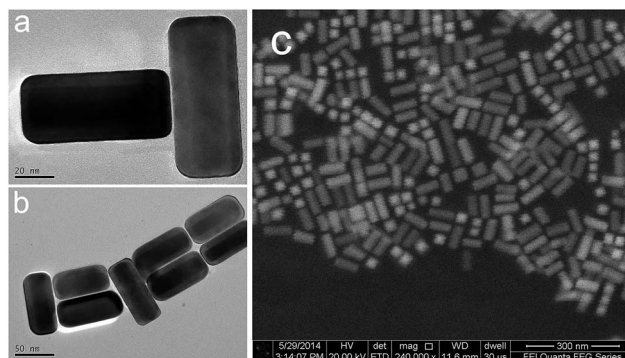


Fig. 2 TEM images of the Au@Ag NRs (a and b) and SEM image of the Au@Ag NRs (c).

the plasmon band, is dependent on the shape and ratio.³⁰ In our experiments, this “rod-like” Au@Ag NR has the longitudinal and the transverse plasmon absorption.

As shown in Fig. 3, there are four strong plasmon resonance peaks regarded as the optical signatures of Au@Ag NRs. To clarify the evolution of surface plasmon bands after the growth of the Ag shell compared with the Au nanorod, the absorption spectrum of initial pure Au NRs (average length and diameter are 65 ± 4 nm and 15 ± 2 nm) was also measured. The longitudinal and transverse plasmon resonance wavelengths of the initial Au nanorod sample dispersed in aqueous solutions are 828 and 521 nm, respectively. After coating the Ag shell with appropriate thickness, the two plasmon peaks blue-shift to 640 and 437 nm, respectively.

Referring to the previous report, because the plasmon resonance wavelength of Ag nanostructures is generally shorter than that of Au nanostructures with the same shape and size, the blue shift of longitudinal surface plasmon wavelength (828 nm to 640 nm) can be understood as arising from both the reduction in the aspect ratio of the Au@Ag nanorods and the effect of the optical properties of Ag shell over Au core. The blue shift of the transverse surface plasmon wavelength (521 nm to 437 nm) can be attributed to the coating of silver because the Ag shell is sufficiently thick to screen the Au on the transverse aspect.

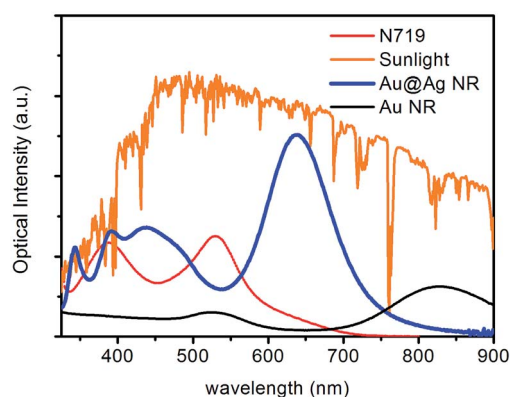


Fig. 3 Solar irradiance spectrum of ASTM G173-03 reference (AM 1.5) and absorption spectrum of the Au@Ag NRs and N719.

The two emerging wavelength (343 nm and 390 nm) are indicative of the surface plasmon mode of Ag. Two peaks appeared after the Ag shell reached a certain thickness, and they red-shift only very slightly as the Ag shell was further increased.²⁵ Thus, the characteristic of the Au@Ag NRs is the tunable longitudinal and transverse plasmon resonance wavelengths of the initial Au NRs. The multiple plasmonic peaks of the nanorods promised an extensive visible-to-NIR coverage.

In addition to the wide absorption feature of the nanorods, another unique characteristic of the metal nanocomposite, the coupling effect between Ag and Au, could enhance the electromagnetic field much larger than single metal nanostructures.³¹ To further confirm the enhanced local field of the Au@Ag NRs, models of the Au nanoparticles sphere (diameter = 45 nm) and the Au nanorod (same dimension as Au@Ag NRs) were built. A theoretical investigation on spatial properties of light trapping by SPR effect was developed to describe its speciality. The finite-difference time-domain method (FDTD) was applied to calculate the LSP field distribution.

Fig. 4 shows the finite-difference time-domain (FDTD) simulation results of the field intensity enhancements of the Au@Ag NRs, Au NRs and Au NPs. The field intensity enhancements were calculated under the excitation at their plasmon wavelengths. It was found that the electrical field intensity of

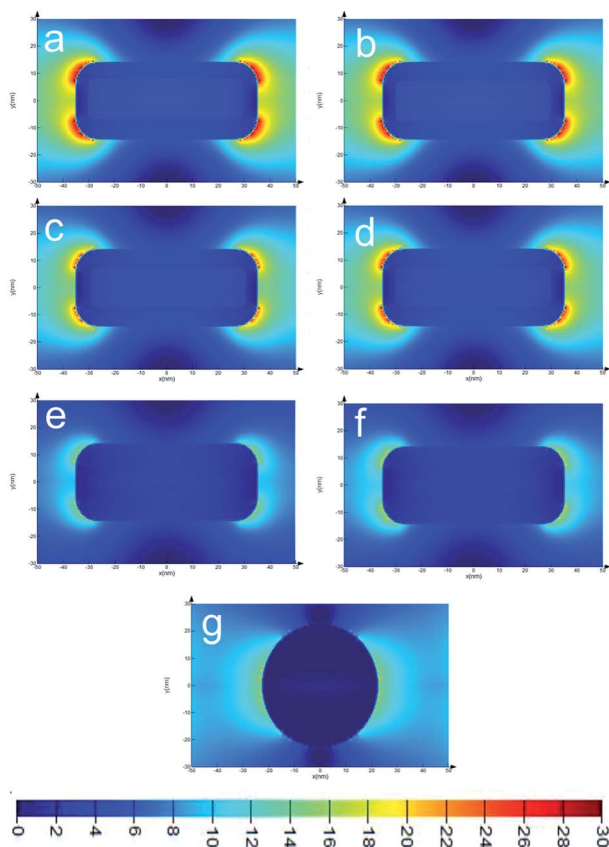


Fig. 4 The calculated distribution of localized electric field intensity around metal nanostructures at plasmon wavelengths: Au@Ag NRs (a) 343 nm (b) 390 nm (c) 437 nm and (d) 640 nm; Ag NRs (e) 530 nm (f) 651 nm; Ag NPs (g) 535 nm.

the Au@Ag NRs is obviously enhanced compared with that of the pure Au NRs and Au NPs. The field intensity enhancement factors along the central length axis are plotted in Fig. 5. The enhancement factors of the Au@Ag NRs are 3.1–5.2 times those of the Au nanorod (at 651 nm) and 4.0–6.8 times those of the Au nanoparticles. This is due to the fact that Ag nanocrystals exhibit considerably stronger electric field enhancements than those of Au nanocrystals,²⁵ and the coupling effect between Ag and Au also contributed to the higher factors. The simulation confirmed the unique local field enhancement effect of the Au@Ag NRs, which plays the role of the research foundation in plasmonic enhanced DSSCs.

As shown in Fig. 3, a considerable overlap between the absorption of N719 and the Au@Ag NRs guaranteed an effective interaction, enhancing the photocatalytic property of the sensitizers. Moreover, the strong absorption of the Au@Ag NRs at the longer wavelength further promoted the sunlight harvesting at red and NIR region.

2.2. Stability and absorption spectroscopy

Referring to the plasmonic nanostructures applied in DSSCs, the chemical and thermal stability of the structure is very important. Bare metal nanoparticles could be easily corroded by the electrolyte, and a thermal deformation will occur after the preparation of photoanode.²¹ Considering this fact, a protective layer around the nanorods is needed before incorporating the nanostructures into DSSCs. In our study, hydrolysis of titanium precursors was used for the formation of a thin TiO₂ shell around the nanorods.¹⁵ Fig. S2† shows the TEM image and Fig. S3† shows the EDX of the TiO₂ shell coated nanorods. As can be seen, the TiO₂ shell coated on the nanorods is very thin (3–4 nm), which is beneficial for readily forming a photoanode film with TiO₂ nanoparticles as well as reducing the corrosion and recombination. As the size and absorption properties of the processed nanorods were almost unchanged (shown in Fig. S3b†), previous discussion of the nanorods were still tenable. Up to this point, the application of the nanorods in DSSCs was realizable and meaningful.

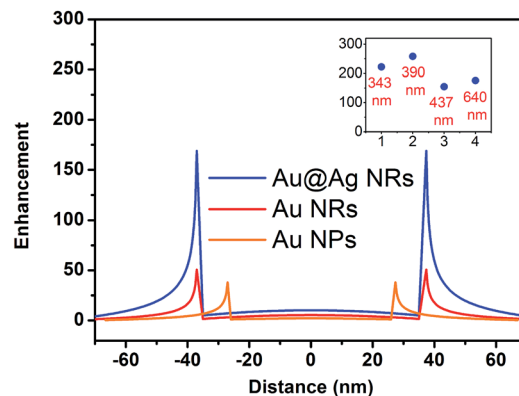


Fig. 5 Electric field intensity enhancement profiles along the length axis and passing through the center of the various metal nanostructures (inset: the electric field intensity enhancement factor of the Au@Ag NRs with four plasmonic wavelengths).

A simple experiment has been developed to evaluate the corrosion resistance of the nanorods to the electrolyte. The same dose of electrolyte was added into a bare Au@Ag NR colloidal solution and treated Au@Ag NR colloidal solution, and the appearance variation was recorded for a certain period of time. As shown in Fig. S4,[†] the color of the bare Au@Ag NR colloidal solution become light and transparent eventually, and we speculated that bare nanorods were easily corroded by the iodide/triiodide redox couple. In contrast, the treated Au@Ag NR colloidal solution maintained a stable state all along, which confirmed the excellent chemical stability of the treated nanorods.

To assess the effect of the Au@Ag NRs on the light absorption of photoanodes, mesoporous TiO₂ films with different amounts of Au@Ag NRs incorporated were prepared (0.00 wt%, 1.28 wt%, 2.49 wt%, 3.68 wt%, and 4.97 wt%). The SEM images of the surface morphologies of various films are shown in Fig. S5.[†] As the amount of the Au@Ag NRs is rather low, all the films showed compact morphologies and smooth surfaces with little difference. In addition, the ratio and the size of Au@Ag NRs exhibit no obvious deformation due to the presence of the TiO₂ protecting layer.

Actually, there are two aspects influencing the thermostability of the nanorods. First, the thin TiO₂ shell coated on the nanorods served as the initial protecting layer; second, after uniformly mixing the nanorods with the TiO₂ paste, the TiO₂ nanoparticles around the NRs could provide an effective insulation effect. Related studies also reported the feasibility of the typical metal nanostructures with thin shell developed in DSSCs.^{32,33} This result demonstrates the good thermostability of the nanorods, and the multiple SPR features of the Au@Ag NRs could still play a role in DSSCs.

UV-Vis absorption spectra of the photoanode films in the absence of dye, with dye adsorbed and with dye desorbed were investigated and discussed in detail. Fig. 6a shows the dye-absence spectra of various films, and an observable SPR band appeared in the absorption spectra of Au@Ag NRs incorporated TiO₂ films. The dye-adsorbed spectra, shown in Fig. 6b, indicated that the enhanced absorption of Au@Ag NRs incorporated TiO₂ films could perform in the entire visible and NIR region. The higher was the concentration of the Au@Ag NRs, the stronger the intensity of absorption was obtained. The significantly enhanced and broadened absorption is mainly attributed to the SPR effect of the Au@Ag NRs. To confirm this inference, the absorption spectra of the dyes N719 desorbed from various films were measured in NaOH solution, and are shown in Fig. 6c. It was found that the intensity of the absorption peak is slightly decreased in the presence of Au@Ag NRs, which clarified that the amount of the dyes in Au@Ag NRs incorporated films was less than that of pure TiO₂ film. This series of discussion strongly supported the views that the enhancement of the absorption is not due to the increase in the amount of dye but the SPR effect. The enhanced electromagnetic field around the Au@Ag NRs improved the interaction with the dye molecules dipoles, and thus resulted in the enhanced light absorption of the dye and more charge carrier generation.^{19,21} Furthermore, a noticeable phenomenon, that is,

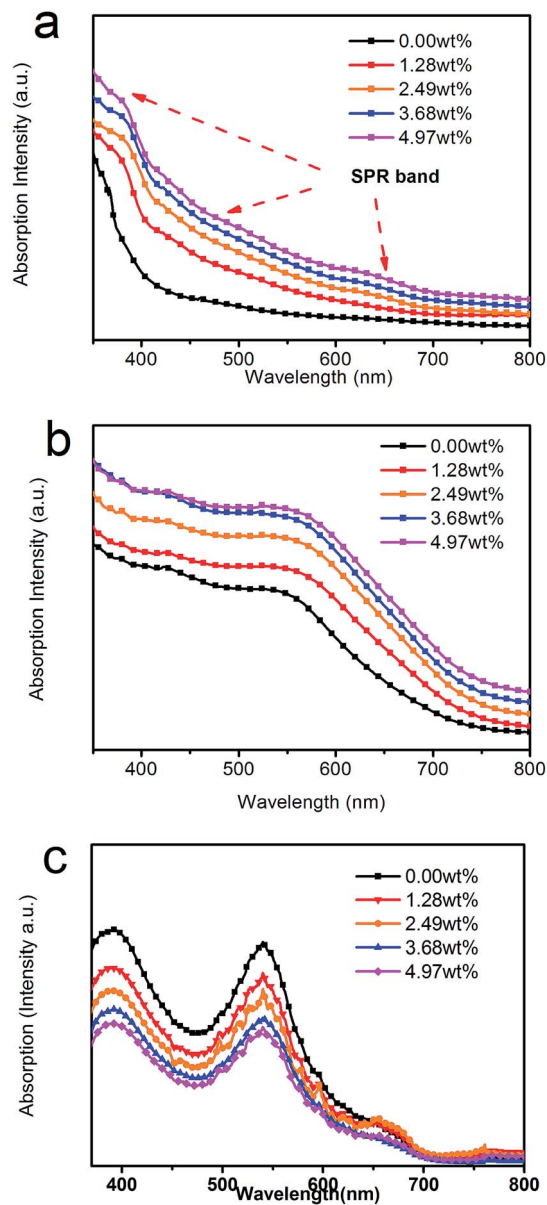


Fig. 6 (a) Absorption spectra of photoanodes with different concentration of Au@Ag NRs (b) absorption spectrum of the different photoanodes with adsorbed dyes. (c) Absorption spectra of the desorbed N719 from dye-loaded TiO₂ film in NaOH solution.

a broadened spectra absorption range, which extends to the red and NIR, was observed. Based on the unique plasmonic properties of the Au@Ag NRs, the enhanced dye absorption and broadened spectrum-absorption range of the photoanodes can be achieved for improving the performance of the DSSCs.

It was noted that when the concentration of the Au@Ag NRs was over 3.68%, the absorption intensity of dye-adsorbed films has almost no increase. Moreover, the amount of dye decreased due to the lower surface area of the film. With the increase of the Au@Ag NRs concentration, the SPR effect of the Au@Ag NRs was enhanced at the expense of the decrease in the adsorption of dye amounts; thus a suitable concentration for maintaining

the balance of the two aspects should be optimized. Only then, the ability of the nanorods can be fully utilized to boost the J_{sc} and the power conversion efficiency of DSSCs.

Here, to further demonstrate the superiority and uniqueness of the Au@Ag NRs, pure Au NRs and Au nanoparticles with same dimension were prepared and applied in DSSCs. The TEM images of Au NPs and Au NRs with TiO₂ shell were shown as Fig. S6.† The absorption spectra of three nanostructures with the same particle number concentration are shown in Fig. S7.† Considering the academic rigour, the particle number concentration of the three nanostructures should be consistent for comparison. The density ratio of single Au@Ag NRs, pure Au NRs and Au nanoparticles was equal to 1 : 1.48 : 1.29. Thus, 3.68% Au@Ag NRs, 5.44% Au NRs, and 4.74% Au NPs were applied into DSSCs.

Fig. 7a shows the absorption of photoanodes with and without three nanostructures at the same particle number concentration, and it was found that enhanced absorption appeared in all nanostructures incorporated films. Pure Au NRs and Au NPs have the similar performance, and Au@Ag NRs was the optimal one.

To further study the enhanced mechanism, the relative changes in the optical absorption ($\Delta OA/OA$) of the various dye-absence photoanodes are shown in Fig. 7b.

Here, the $\Delta OA/OA$ was defined as:

$$\Delta OA/OA = (\text{Abs (photoanode with nanostructure)} - \text{Abs (pure photoanode)}) / \text{Abs (pure photoanode)}$$

With regards to the pure Au NRs and Au NPs, the relative enhancement can be observed, and the enhancement band coincided with the LSPR band position of single nanoparticles, respectively (Fig. 7b). It is noted that the performance of the Au@Ag NRs was distinctive. The $\Delta OA/OA$ of Au@Ag NRs was significantly broadened and enhanced compared to pure Au nanostructures, and the enhancement band in the range of 350–800 nm with three bands (405 nm, 462 nm, and 635 nm) is roughly in accordance with the plasmonic features of the single Au@Ag NRs. The results clarified that the coupling effect between Ag and Au could provide the capability of achieving strong localized field as well as extending the absorption to the red and NIR region. This advantage effectively promoted the absorption of photoanode compared with traditional metal nanostructures.

2.3. Photovoltaic performance of DSSCs

To investigate the properties of Au@Ag NRs on the performance of DSSCs, the photocurrent–voltage (I – V) and incident photon-to-current conversion efficiency (IPCE) characteristics of DSSCs with different TiO₂ photoanodes were discussed and shown in

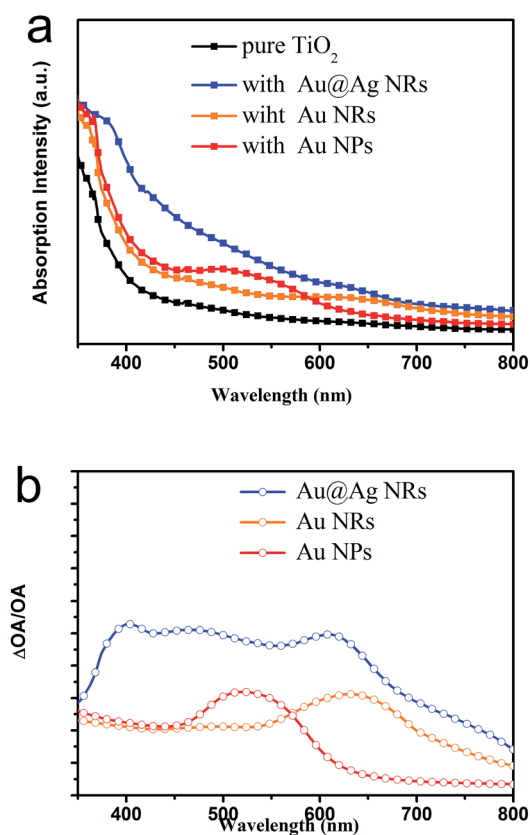


Fig. 7 UV-Vis absorption spectra of different photoanode films (a) and relative changes in optical absorption ($\Delta OA/OA$) of different photoanode films (b).

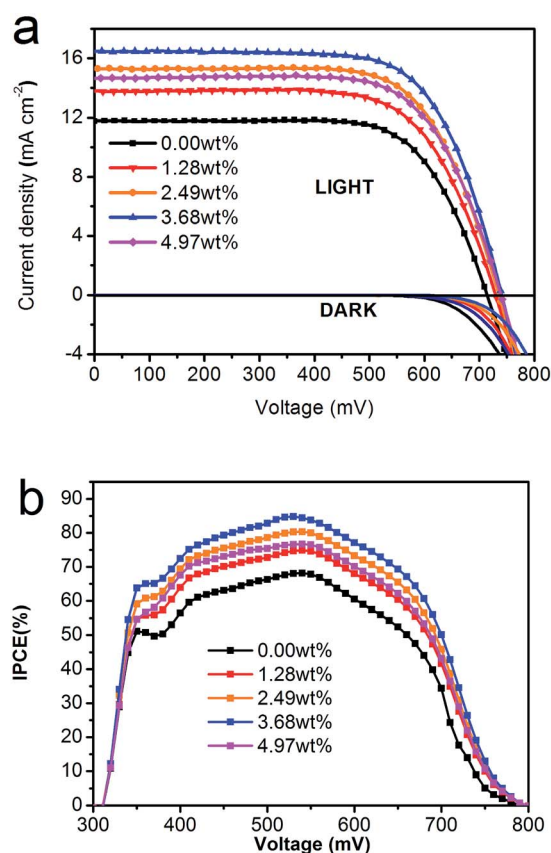


Fig. 8 (a) I – V and (b) IPCE characteristic of DSSCs with various TiO₂ photoanodes.

Table 1 Photovoltaic characteristics of DSSCs with various TiO₂ photoanodes

Group	V _{oc} (mV)	J _{sc} (mA cm ⁻²)	FF	η (%)	R _{ct} (Ω)
Pure TiO ₂	711	11.69	0.704	5.91	50.21
1.28%-Au@Ag NRs	728	13.74	0.698	6.88	54.34
2.49%-Au@Ag NRs	730	15.31	0.699	7.78	61.67
3.68%-Au@Ag NRs	729	16.53	0.701	8.43	67.50
4.97%-Au@Ag NRs	727	14.56	0.705	7.50	57.07

Fig. 8a and b, and the performance parameters were summarized in Table 1.

It was found that the photocurrent has an obvious increase tendency with the concentration of Au@Ag NRs. The optimized J_{sc} of 16.53 mA cm⁻² and PCE of 8.43% were achieved in the DSSC with the content of 3.68 wt%, which exhibit a 40% enhancement of PCE in comparison with that in the DSSC with a pure TiO₂ photoanode. The enhancement of J_{sc} can be mainly attributed to the improvement of light harvesting efficiency in the visible and NIR region by plasmon-enhanced excitation. As the plasmonic wavelength of Au@Ag NRs has a considerable overlap with the strong energy of the sunlight, the effective SPR effect can be ensured. Owing to the coupling effect, remarkably enhanced localized electromagnetic fields can be obtained. Then, the dye molecules around the neighbouring Au@Ag NRs could absorb more photons and convert the photons to charge carriers.

Another factor influencing the J_{sc} was the charge transport–recombination effect of the Au@Ag NRs. The apparent and uniform Fermi level of the metal nanostructure/TiO₂ interface could form electron–hole separation centers,³⁴ and this steady state of semiconductor–metal nanostructure contact could accelerate the movement of photo-generated electrons from excited dyes to TiO₂ nanoparticles, thus reducing the recombination of carriers and increasing the J_{sc}.³⁵

The dark-current reflects the recombination of charges in the conduction band of TiO₂ with triiodide to some extent. Fig. 8a shows the dark-current curves of different DSSCs. Compared to the DSSCs based on the pure TiO₂ film, the dark current of the DSSCs with Au@Ag NRs was significantly decreased, which can be attributed to the suppression of the recombination between triiodide and electrons in the TiO₂ network.

After reaching the maximum value at 3.68 wt%, the J_{sc} and PCE of the devices decreased along with the increase of the concentration of Au@Ag NRs. As the light absorption efficiency was almost unchanged over 3.68 wt%, the change of J_{sc} was probably associated with the role of the electrical properties. Though the introduction of the nanorods was conducive to the suppression of the charge recombination for DSSCs, the excess concentration of nanorods probably induced the flaw and the aggregation of TiO₂ film (shown in Fig. S5†). Then, the capability of the reducing recombination was weakened. The advantage of the increased light harvesting effect is offset by the recombination, and the dark current curves show the same tendency with the J_{sc}, further indicating the charge recombination was influenced by the Au@Ag NRs.

The incident photon-to-electron conversion efficiency (IPCE) of DSSCs is shown in Fig. 8b. As the consequence of both improved light-harvesting efficiency and electron injection–collection efficiency at the photoanodes, the tendency of IPCE is consistent with the trend of J_{sc}. In the visible region, the significantly improved of IPCE in Au@Ag NRs incorporated DSSCs can be observed, reflecting the sensitizers around the nanorods harvesting more photons. In addition to this, the IPCE of DSSCs with Au@Ag NRs show obvious broadening at longer wavelengths (>600 nm), as compared with that of the DSSCs with pure TiO₂. As the longitudinal plasmon absorption around 640 nm of the Au induced the light trapping, it could enhance optical density for improving photocurrent generation in this region. In general, in addition to the strong interaction with the dyes, the presence of the Au@Ag NRs also contributed to the long wavelength harvesting of the sunlight in the devices.

For comparison, *I*–*V* and IPCE of DSSCs with Au@Ag NRs, Au NRs and Au NPs at the same particle concentration were discussed and are shown in Fig. S8.† Compared to the efficiency of the reference device with 5.91%, the efficiency of devices with Au@Ag NRs, pure Au NRs and pure Au NPs are 8.43%, 7.62% and 7.51%, respectively. DSSCs with two types of NRs exhibits an enhancement of IPCE over a broad spectral range than the device with pure Au NPs, and the device with Au@Ag NRs has the optimal performance. This result further clarified the broadened and strong plasmonic absorption enhancement of the Au@Ag NRs.

2.4. Electrical properties of DSSCs

Previous discussion of absorption and *I*–*V* properties illustrated that the substantially improved performance was dominated by the optical aspect *via* the SPR effect. In addition, the introduction of Au@Ag NRs into photoanode also had impact on the charge generation, separation, and recombination processes. Perhaps the electrical contribution to the final performance was relatively negligible owing to the low concentration of Au@Ag NRs. In fact, fully understanding the mechanism was beneficial to develop a more effective application of the Au@Ag NRs in the DSSCs. To further clarify the role of the Au@Ag NRs in electrodynamic process, a schematic of the equilibration of the apparent Fermi level of the NRs/TiO₂ interface and the charge transfer–separation process is shown in Fig. 9, and detailed discussion is as follows.

Metal nanoparticles have been known to play an important role in semiconductor-assisted photocatalytic reduction processes, and the capability to promote interfacial electron–hole transfer has been well studied.^{13,36} Previous reports indicate that the electron transfer from neighboring semiconductor to the metal nanoparticle is an ultrafast process.^{34,37} As for our experiment, the Fermi energy of both the Au and Ag lies below the conduction band (CB) of TiO₂.³⁸ When the devices are operated under illumination, photoelectrons can be generated from excited dyes and TiO₂. Due to the deep Fermi level of Ag and Au, metal NRs is capable of accepting electrons from the neighboring TiO₂/dye particles and undergo Fermi level equilibration.¹⁵ Considering the unique electron storage capability of

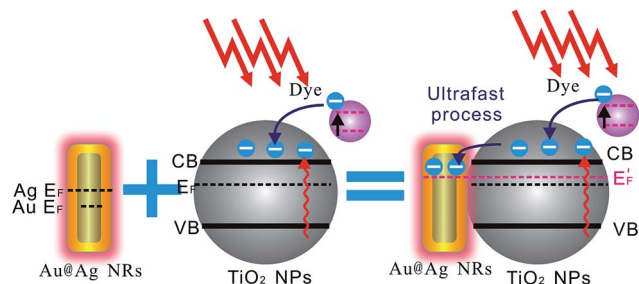


Fig. 9 Schematic illustration of the equilibration of the apparent Fermi level of the NRs/TiO₂ interface and the charge transfer–separation process.

the metal nanostructure,¹³ electrons quickly accumulated in the metal nanorods until reaching a critical point. After undergoing electron equilibration, the stored electrons assist in maintaining a more negative uniform Fermi level of metal/TiO₂ composite than the pristine TiO₂;¹⁵ this process could reflect the slightly improved open voltage of the DSSCs with Au@Ag NRs (shown in Fig. 8a).

In addition, the uniform Fermi level at the metal/TiO₂ interface could promote the charge transport–separation process.^{35,39} Recent studies indicate that the electron transfer from a semiconductor to a metal nanoparticle is an ultrafast process.³⁷ The electron storage property of metal can be beneficially used to improve photoelectrochemistry, and the noble metals, such as Au and Ag, could possess electron storage properties, which in turn facilitates improved charge separation–transport in semiconductor–metal composite systems.^{40,41} The metal/TiO₂ interface will form electron–hole separation centers, which would be beneficial in improving the movement of photo-generated electrons shuttling through the porous TiO₂ network, reducing the recombination of electrons and holes, thus increasing the photocurrent.¹⁶

To confirm the capability of charge separation by Au@Ag NRs, the PL spectra of pure TiO₂ and Au@Ag NRs incorporated films are shown in Fig. 10. PL spectra are often used to study the surface processes involving electron–hole recombination of semiconductors.⁴² The broad-band emission around 425 nm was assigned to the recombination of photoexcited holes with electrons occupying the singly ionized oxygen vacancies in TiO₂. The PL intensity in Au@Ag NRs incorporated film has an obvious reduction compared to that of the pure TiO₂ film, which indicated that the recombination of electron–hole pairs in the TiO₂ film decorated with Au@Ag NRs has been suppressed effectively.

When operating either the real device or the photoanode without dyes, a charge transporting–separating process enduring at the metal–semiconductor interface was inevitable. The difference in the real device was the generated-photo-carrier, mainly from the excited dyes. Therefore, the PL measurement could demonstrate the capability of the charge separation by Au@Ag NRs at metal–semiconductor interface, which indirectly clarified the effect of the NRs in real DSSCs. The results of the dark-current measurement also exhibit the restraining recombination by the Au@Ag NRs.

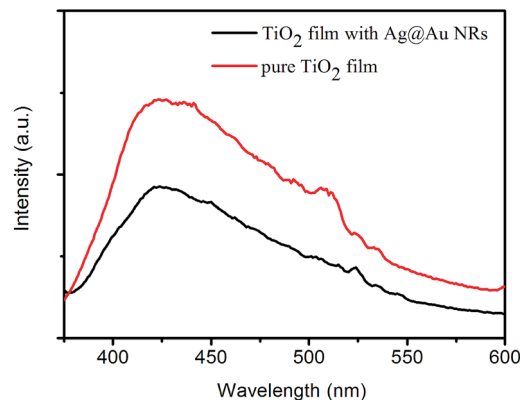


Fig. 10 Photoluminescence (PL) spectra of pure TiO₂ film and Au@Ag NRs-modified TiO₂ film.

Electrochemical impedance spectroscopy was introduced as a further proof to reveal the charge transport–recombination processes in DSSCs. With the established equivalent circuits depicted in the Fig. 11a, the kinetics of electrical transport and recombination can be considered in terms of a combination of the complex impedance Z_1 and Z_2 .⁴³ The impedance spectra of DSSCs (Nyquist plot) under dark condition are shown in Fig. 11b. From left to the right, the first semicircle portion (Z_1) in the Nyquist plots corresponds to the reduction reaction at the counter electrode, and the second semicircle (Z_2) was assigned to the charge recombination at the TiO₂/sensitizers/electrolyte interface. In our study, considering that the introduction of metal nanostructures mainly affects the TiO₂/sensitizers/electrolyte interface, resistance R_{ct} (real part of Z_2) is discussed and summarized in Table 1.

Under dark conditions, the electron process of TiO₂/sensitizers/electrolyte interface is only the recombination between

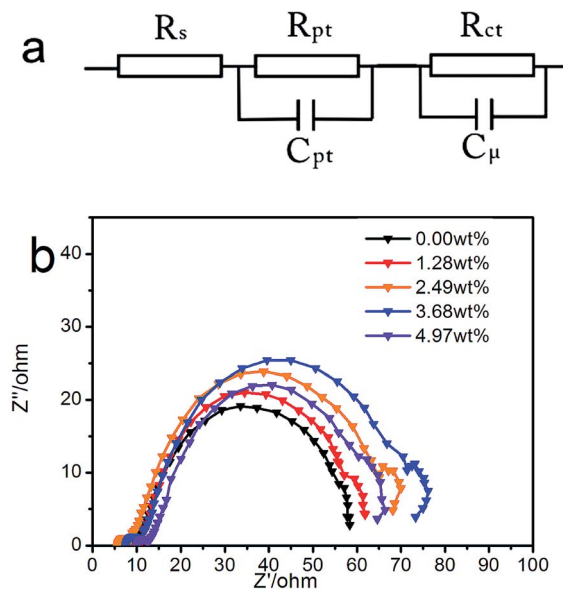


Fig. 11 Electrochemical impedance spectra of DSSCs (a) equivalent circuit model (b) Nyquist plots of electrochemical impedance spectra of different DSSCs.

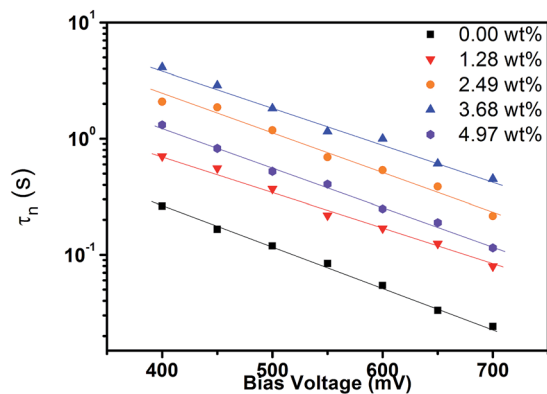


Fig. 12 Electron residence time (τ_n) in different DSSCs.

electrons and I^-/I_3^- in the electrolyte.⁴⁴ The larger the value of R_{ct} was, the slighter the electron recombination at the TiO_2 /sensitizers/electrolyte interface was. Compared to the DSSC with pure TiO_2 film, the R_{ct} value of the DSSCs with Au@Ag NRs was increased. A larger R_{ct} reflected a lower dark current generated from charge recombination with the triiodide ion at the TiO_2 /dye/electrolyte interface. Here, the Au@Ag NRs act as electron-hole separation centers due to the Schottky barriers at the metal/ TiO_2 interface, successfully reducing charge recombination reaction. It is noted that the maximum value of R_{ct} was obtained at 3.68 wt%, and this phenomenon further demonstrated the inference that the only appropriate concentration ensured the optimal recombination-reduced ability.

Electron residence lifetime (τ) derived from the EIS measurements with different bias voltage provided further explanation on the suppression of charge recombination in DSSCs. As is shown in Fig. 12, compared to the DSSCs with pure TiO_2 , DSSCs with Au@Ag NRs exhibit a longer electron lifetime, revealing that the presence of the nanorods was in favour of suppressing the charge recombination. Moreover, the lifetime show an increasing-decreasing trend with the increase of the Au@Ag NRs, with the longest lifetime at 3.68 wt%, in good agreement with the dark-current and $I-V$ curves.

Electron residence lifetimes of DSSCs with different metal nanostructures were also investigated. As shown in Fig. S9,[†] DSSCs with three nanostructures exhibit longer lifetimes than the reference DSSC, which clarified that the presence of the metal nanostructures was conducive to the suppression of charge recombination. It is noted that the lifetimes of three plasmonic DSSCs had little difference at the same particle concentration because the size of the metal nanoparticle affects the electron storage capacity. The comparison explained that the efficiency of DSSCs was mainly influenced by the plasmonic absorption enhancement property, which precisely is the unique advantage of the Au@Ag NRs.

3. Conclusion

In this article, a unique core-shell Au@Ag NRs is prepared and applied in DSSCs. It is found that the use of plasmonic nanorods significantly improved the performance of DSSCs. By

efficiently affecting the sensitizers and converting low energy sunlight into electricity, an optimal performance of device with nanorods reaching up to 8.43% can be obtained, which was almost 40% higher than the device without Au@Ag NRs. Considering that the optical property of the nanorods can be tuned *via* the aspect ratio, beyond the development of strong plasmonic absorption at visible region, effective light harvesting at longer wavelengths is expected to be achieved *via* regulating the ratio. This plasmonic approach has a huge potential to act as an assistance and supplement to various universal sensitizers for higher LHE, and further research is needed to utilize the novel prospects on various areas. In general, we hope that our study could provide new ways to develop applications on organic solar cells, CIGS thin film solar cells and perovskite solar cells.

4. Experimental section

4.1. Synthesis of (Au core)-(Ag shell) nanorods, Au nanorods and Au nanoparticles

AuNRs were synthesized *via* a seed mediated method reported by Murphy *et al.*⁴⁵ With regards to the control of the thickness of the Ag shell, different concentration of $AgNO_3$ and ascorbic acid led to the sized-tunable (Au core)-(Ag shell) nanorods.²⁵ The as-synthesized Au NRs solution was centrifuged at 10 000 rpm for 60 min, and then redispersed in aqueous CTAC solutions (0.08 M) at the same volume. 0.45 mL $AgNO_3$ (0.008 M) were subsequently added into the 2 mL Au nanorod solution, followed by the addition of 0.015 mL ascorbic acid solutions (0.1 M). The resultant solutions were kept in an isothermal oven at 60 °C for 4 h. Then, the bare (Au core)-(Ag shell) nanorods were obtained.

The initial Au@Ag NRs were dispersed into deionized water and centrifuged at 10 000 rpm, and this process was repeated several times for removing the residual CTAC. Then, 0.1 g of the precipitate was added into 30 mL deionized water. 0.012 g titanium tetraisopropoxide (TTIP) as the TiO_2 precursor was added in the solution and stirring was continued for an additional 30 min at 60 °C to ensure the completion of the reaction. Au@Ag NRs with thin TiO_2 shell layer were then obtained. The solution was washed several times and centrifuged at 6000 rpm to remove TTIP. The final precipitation was air dried and doped in pure TiO_2 paste with various ratios.

Here, the ratio between TTIP and Au@Ag NRs mainly determined the thickness of the TiO_2 , and the dispersion and washing process influenced the integrity of the coating.

Pure Au nanorods were also synthesized *via* a seed mediated method reported by Murphy *et al.* Pure Au nanoparticles were synthesized *via* the method of Liz-Marzan *et al.*⁴⁶ The TiO_2 coating process is similar to the TiO_2 coated Au@Ag NRs.

4.2. Fabrication of photoanodes and DSSCs

Glass substrates coated FTO (Nippon Sheet Glass, Japan, 2.2 mm thickness, $14 \Omega \square^{-1}$) were cleaned in a detergent solution for 30 min in an ultrasonic bath, and rinsed with deionized water, isopropanol and EtOH for 30 min. The pure TiO_2 pastes were prepared by TiO_2 powder (Degussa, P25), and different

photoanodes were synthesized by stirring various amounts of treated Au@Ag NRs into the pure TiO₂ pastes according to a series of mass ratios (Au@Ag NRs : P25 = 0.00%, 1.28%, 2.49%, 3.68%, and 4.97%), (Au NRs : P25 = 5.44%), (Au NPs : P25 = 4.74%). Then, the seven kinds of transparent TiO₂ pastes were screen-printed onto the FTO as the transparent layer, and then the coated films were dried at temperature of 125 °C for 6 min. This screen-printing procedure with the paste was repeated to obtain an appropriate thickness of 8 μm of TiO₂ for the working electrode. The coated substrates were thermally treated under an air flow at 325 °C for 5 min, 375 °C for 10 min, 450 °C for 15 min and 500 °C for 15 min. After cooling to 80 °C, the TiO₂ electrode was stained by immersing it into a dye solution containing N719 sensitizer (300 μm) in a mixture of acetonitrile and *tert*-butyl alcohol (volume ratio: 1 : 1) overnight. The TiO₂ photoanodes adsorbed dye and 2 nm Pt counter electrodes were assembled into a sealed sandwich-type cell by a 60 μm hot-melt ionomer film Bynel (Dupont) as a spacer between the electrodes. A drop of the electrolyte solution, 0.6 M 1-butyl-3-methyl imidazolium iodide (BMII), 0.03 M I₂, 0.02 M LiI, 0.10 M guanidinium thiocyanate and 0.5 M 4-*tert*-butylpyridine in a mixture of acetonitrile and valeronitrile (volume ratio, 85 : 15), was injected into the cell.

4.3. Characterization

The morphology of the Au@Ag NRs was investigated by scanning electron microscopy (SEM) (Quanta 250, FEI) and transmission electron microscopy (TEM) (2100, JEOL). The chemical species of the Au@Ag NRs were analyzed by energy-dispersive X-ray spectroscopy (EDX) (EDAX, Quanta 250, FEI). The crystalline structure of the various TiO₂ films was determined by X-ray diffraction (XRD) (D/MAX-2400, Rigaku, Japan). The UV-Vis absorption spectra of the Au@Ag NRs were obtained on a UV-Vis spectrophotometer (Fluoromax 4, HORIBA Jobin Yvon, USA). The incident photon-to-current conversion efficiency (IPCE) was evaluated by a solar cell quantum efficiency measurement system (SolarCellScan 100, Zolix instruments. Co. Ltd). The photocurrent density–voltage characteristics were evaluated by a AAA solar simulator (XES-301S, SAN-EI Electric. Co. Ltd.), AM 1.5G illumination (100 mW cm⁻² in intensity), and a Keithley digital source meter (Model 2602). Electrochemical impedance spectra (EIS) of the cells were evaluated using CHI-660D over the frequency range of 0.1 Hz to 100 KHz under the conditions of open circuit below 100 mW cm⁻². All the cells had an active area about 0.25 cm².

Acknowledgements

This work was financially supported by Basic Research Program of China (2013CB328705), National Natural Science Foundation of China (Grant nos 61275034, 61106123), Ph.D. Programs Foundation of Ministry of Education of China (Grant no. 20130201110065); Fundamental Research Funds for the Central Universities (Grant no. xjj2012087). The SEM work was performed at International Center for Dielectric Research (ICDR),

Xi'an Jiaotong University, Xi'an, China; the authors also thank Ms Dai for her help in using SEM.

Notes and references

- 1 B. Oregan and M. Gratzel, *Nature*, 1991, **353**, 737–740.
- 2 S. Mathew, A. Yella, P. Gao, R. Humphry-Baker, B. F. E. Curchod, N. Ashari-Astani, I. Tavernelli, U. Rothlisberger, M. K. Nazeeruddin and M. Gratzel, *Nat. Chem.*, 2014, **6**, 242–247.
- 3 B. E. Hardin, H. J. Snaith and M. D. McGehee, *Nat. Photonics*, 2012, **6**, 162–169.
- 4 M. Gratzel, *Nature*, 2001, **414**, 338–344.
- 5 A. Yella, H. W. Lee, H. N. Tsao, C. Y. Yi, A. K. Chandiran, M. K. Nazeeruddin, E. W. G. Diau, C. Y. Yeh, S. M. Zakeeruddin and M. Gratzel, *Science*, 2011, **334**, 629–634.
- 6 T. W. Hamann, R. A. Jensen, A. B. F. Martinson, H. Van Ryswyk and J. T. Hupp, *Energy Environ. Sci.*, 2008, **1**, 66–78.
- 7 Y. M. Cao, Y. Bai, Q. J. Yu, Y. M. Cheng, S. Liu, D. Shi, F. F. Gao and P. Wang, *J. Phys. Chem. C*, 2009, **113**, 6290–6297.
- 8 Z. S. Wang, Y. Cui, K. Hara, Y. Dan-Oh, C. Kasada and A. Shinpo, *Adv. Mater.*, 2007, **19**, 1138–1141.
- 9 J. H. Yum, P. Walter, S. Huber, D. Rentsch, T. Geiger, F. Nuesch, F. De Angelis, M. Gratzel and M. K. Nazeeruddin, *J. Am. Chem. Soc.*, 2007, **129**, 10320–10321.
- 10 P. Y. Reddy, L. Giribabu, C. Lyness, H. J. Snaith, C. Vijaykumar, M. Chandrasekharam, M. Lakshmikantam, J. H. Yum, K. Kalyanasundaram, M. Gratzel and M. K. Nazeeruddin, *Angew. Chem., Int. Ed.*, 2007, **46**, 373–376.
- 11 Q. Q. Miao, L. Q. Wu, J. N. Cui, M. D. Huang and T. L. Ma, *Adv. Mater.*, 2011, **23**, 2764–2768.
- 12 G. K. Mor, J. Basham, M. Paulose, S. Kim, O. K. Varghese, A. Vaish, S. Yoriya and C. A. Grimes, *Nano Lett.*, 2010, **10**, 2387–2394.
- 13 A. Takai and P. V. Kamat, *ACS Nano*, 2011, **5**, 7369–7376.
- 14 H. Dong, Z. X. Wu, Y. C. Gao, A. El-Shafei, B. Jiao, Y. Dai and X. Hou, *Org. Electron.*, 2014, **15**, 1641–1649.
- 15 H. Choi, W. T. Chen and P. V. Kamat, *ACS Nano*, 2012, **6**, 4418–4427.
- 16 K. M. Guo, M. Y. Li, X. L. Fang, X. L. Liu, B. Sebo, Y. D. Zhu, Z. Q. Hu and X. Z. Zhao, *J. Power Sources*, 2013, **230**, 155–160.
- 17 Y. Li, H. Wang, Q. Y. Feng, G. Zhou and Z. S. Wang, *Energy Environ. Sci.*, 2013, **6**, 2156–2165.
- 18 Z. B. Tian, L. Q. Wang, L. S. Jia, Q. B. Li, Q. Q. Song, S. Su and H. Yang, *RSC Adv.*, 2013, **3**, 6369–6376.
- 19 M. D. Brown, T. Suteewong, R. S. S. Kumar, V. D'Innocenzo, A. Petrozza, M. M. Lee, U. Wiesner and H. J. Snaith, *Nano Lett.*, 2011, **11**, 438–445.
- 20 X. N. Dang, J. F. Qi, M. T. Klug, P. Y. Chen, D. S. Yun, N. X. Fang, P. T. Hammond and A. M. Belcher, *Nano Lett.*, 2013, **13**, 637–642.
- 21 S. D. Standridge, G. C. Schatz and J. T. Hupp, *J. Am. Chem. Soc.*, 2009, **131**, 8407–8409.

- 22 H. Dong, Z. X. Wu, Y. C. Gao, A. El-Shafei, S. Y. Ning, J. Xi, B. Jiao and X. Hou, *Org. Electron.*, 2014, **15**, 2847–2854.
- 23 F. L. Su, T. Wang, R. Lv, J. J. Zhang, P. Zhang, J. W. Lu and J. L. Gong, *Nanoscale*, 2013, **5**, 9001–9009.
- 24 S. Muduli, O. Game, V. Dhas, K. Vijayamohan, K. A. Bogle, N. Valanoor and S. B. Ogale, *Solar Energy*, 2012, **86**, 1428–1434.
- 25 R. B. Jiang, H. J. Chen, L. Shao, Q. Li and J. F. Wang, *Adv. Mater.*, 2012, **24**, Op200–Op207.
- 26 B. Pietrobon, M. McEachran and V. Kitaev, *ACS Nano*, 2009, **3**, 21–26.
- 27 W. Ni, X. Kou, Z. Yang and J. F. Wang, *ACS Nano*, 2008, **2**, 677–686.
- 28 Z. S. Yang and H. T. Chang, *Nanotechnology*, 2006, **17**, 2304–2310.
- 29 Y. U. Xiang, X. C. Wu, D. F. Liu, Z. Y. Li, W. G. Chu, L. L. Feng, K. Zhang, W. Y. Zhou and S. S. Xie, *Langmuir*, 2008, **24**, 3465–3470.
- 30 Y. Okuno, K. Nishioka, A. Kiya, N. Nakashima, A. Ishibashi and Y. Niidome, *Nanoscale*, 2010, **2**, 1489–1493.
- 31 N. J. Borys, M. J. Walter and J. M. Lupton, *Phys. Rev. B: Condens. Matter Mater. Phys.*, 2009, **80**.
- 32 K. M. Guo, M. Y. Li, X. L. Fang, X. L. Liu, Y. D. Zhu, Z. Q. Hu and X. Z. Zhao, *J. Mater. Chem. A*, 2013, **1**, 7229–7234.
- 33 S. Chang, Q. Li, X. D. Xiao, K. Y. Wong and T. Chen, *Energy Environ. Sci.*, 2012, **5**, 9444–9448.
- 34 C. Harris and P. V. Kamat, *ACS Nano*, 2010, **4**, 7321–7330.
- 35 R. A. Naphade, M. Tathavadekar, J. P. Jog, S. Agarkar and S. Ogale, *J. Mater. Chem. A*, 2014, **2**, 975–984.
- 36 P. V. Kamat, *J. Phys. Chem. Lett.*, 2012, **3**, 663–672.
- 37 R. Katoh, A. Furube, K. Yamanaka and T. Morikawa, *J. Phys. Chem. Lett.*, 2010, **1**, 3261–3265.
- 38 M. Jakob, H. Levanon and P. V. Kamat, *Nano Lett.*, 2003, **3**, 353–358.
- 39 Y. Y. Lou, S. Yuan, Y. Zhao, P. F. Hu, Z. Y. Wang, M. H. Zhang, L. Y. Shi and D. D. Li, *Dalton Trans.*, 2013, 5330–5337.
- 40 P. V. Kamat and B. Shanghavi, *J. Phys. Chem. B*, 1997, **101**, 7675–7679.
- 41 G. Merga, L. C. Cass, D. M. Chipman and D. Meisel, *J. Am. Chem. Soc.*, 2008, **130**, 7067–7076.
- 42 M. D. Ye, D. J. Zheng, M. Q. Lv, C. Chen, C. J. Lin and Z. Q. Lin, *Adv. Mater.*, 2013, **25**, 3039–3044.
- 43 L. Y. Han, N. Koide, Y. Chiba and T. Mitate, *Appl. Phys. Lett.*, 2004, **84**, 2433–2435.
- 44 R. Gao, G. D. Niu, L. D. Wang, B. B. Ma and Y. Qiu, *Acta Phys.-Chim. Sin.*, 2013, **29**, 73–81.
- 45 N. R. Jana, L. Gearheart and C. J. Murphy, *Adv. Mater.*, 2001, **13**, 1389–1393.
- 46 J. Rodriguez-Fernandez, J. Perez-Juste, F. J. G. de Abajo and L. M. Liz-Marzan, *Langmuir*, 2006, **22**, 7007–7010.